# Toward Maximally Electromagnetically Chiral Scatterers at Optical Frequencies

X. Garcia-Santiago,* M. Hammerschmidt, J. Sachs, S. Burger, H. Kwon, M. Knöller, T. Arens, P. Fischer, I. Fernandez-Corbaton, and C. Rockstuhl

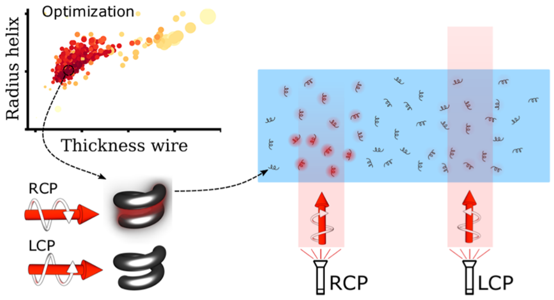

**ABSTRACT:** Designing objects with predefined optical properties is a task of fundamental importance for nanophotonics, and chirality is a prototypical example of such a property, with applications ranging from photochemistry to nonlinear photonics. A measure of electromagnetic chirality with a well-defined upper bound has recently been proposed. Here, we optimize the shape of silver helices at discrete frequencies ranging from the far-infrared to the optical band. Gaussian process optimization, taking into account also shape derivative information on the helices scattering response, is used to maximize the electromagnetic chirality. We show that the theoretical designs achieve more than 90% of the upper bound of em-chirality for wavelenghts 3 $\mu$m or larger, while their performance decreases toward the optical band. We fabricate and characterize helices for operation at 800 nm and identify some of the imperfections that affect the performance. Our work motivates further research both on the theoretical and fabrication sides to unlock potential applications of objects with large electromagnetic chirality at optical frequencies, such as helicity filtering glasses. We show that, at 3 $\mu$m, a thin slab of randomly oriented helices can absorb 99% of the light of one helicity while absorbing only 10% of the opposite helicity.

**KEYWORDS:** *electromagnetic chirality, Bayesian optimization, T-matrix, shape optimization, nanostructure fabrication, polarization filter*

## INTRODUCTION

Chirality is a property usually judged only through geometrical considerations. The definition for chirality has been put forward by Lord Kelvin.[1] It states that an object is chiral if it cannot be superimposed onto its mirror image, called an enantiomer, by any means of rotation or translation. In contrast, if the objects can be superimposed on each other, they are considered achiral.

The concept of chirality is important for many scientific disciplines. In chemistry, for example, many molecules are chiral, and certain reactions are only triggered by one of the two enantiomers. As most physical properties of the two enantiomers are identical, we can only distinguish them by probing their response with another chiral object or a chiral interaction. Light is an excellent tool for this purpose as chiral molecules or any other chiral object interact with electromagnetic fields differently depending on the handedness of the illumination.[2] The helicity of the field expresses the handedness. For a single plane wave, it concerns left- or right-handed circularly polarization.

The differential interaction of electromagnetic fields with chiral objects is used to design devices that increase the cross-section of a certain molecular reaction,[3−5] molecular interaction,[6−14] or that can filter polarization.[15,16] Suppose one aims to design a device that maximizes the difference in the interaction with fields of a specific handedness. In this case, it could be reasonable to think about maximizing the chirality of the object on the ground of geometrical consideration. The first problem with this idea is that it has already been shown that a consistent measure for quantifying the typical geometrical definition of chirality does not exist.[17] Many proposals to measure the chirality of an object have been put forward, for example, in ref 18, but all of them present certain inconsistencies.[19] A measure for the electromagnetic chirality, $\chi$, was recently proposed to lift that issue.[20] This measure assigns a degree of electromagnetic chirality, em-chirality for brevity, to objects based on how differently the object interacts with all the possible illumination fields of different helicities. While the definition of $\chi$ encompasses general illuminations, a single frequency version can be obtained by restricting the illumination to monochromatic fields.

The em-chirality is consistent with the chirality of an object. Any achiral object will have a $\chi$ value of zero at all frequencies.

The link between the em-chirality and further electromagnetic quantities, such as circular dichroism, and an interaction-based measure of geometrical chirality was studied in ref 21.

One salient property of $\chi$ is that its upper bound is given by the total interaction cross-section of the object. The latter can be used to normalize $\chi$. The values of the normalized measure, $\overline{\chi}$, range from 0 to 1. The upper bound at 1 gives rise to the notion of maximally em-chiral objects. If an object is maximally em-chiral at some frequency, this object would be invisible to any field of one of the two polarization handedness at such a frequency. In other words, it would be invisible to all the eigenstates of the helicity operator with one of its two eigenvalues, see ref 22, Chapter 8. Thus, this object would be ideal for angle-independent polarization filters, as proposed in ref 20, and it would also be a cornerstone for systems requiring large interaction differences with the two helicities.

The question of whether one can obtain these objects, in reality, remained, however, open. Analytical designs to achieve such objects can be approached by assuming perfect electric conductors and assuming that the object is made from arbitrarily thin wires.[23] Concerning real-world objects, it has been shown that, by considering these analytical designs, a helix made from silver could be designed that shows a $\overline{\chi}$ above 0.9, however, only at far-infrared wavelengths (e.g., at 200 $\mu$m[20]). Up to now it is not clear if objects with high $\overline{\chi}$ can be obtained at optical frequencies or in the near-infrared, where silver is no longer a perfect conductor. The onset of a kinetic inductance in the metal usually prevents the extrapolation of analytical designs at radiofrequencies toward the visible.

In this work, we look into whether it is possible to design scatterers with a high em-chirality at frequencies as large as the optical frequencies using suitable techniques from the field of computational material design. We limit the search to silver helices. The reason for that is that helices are canonical chiral objects that have been shown to present strong differences in their interaction with fields of different handedness.[15,23−28] High values of em-chirality have already been shown for helices. Limiting the search to helices also simplifies the optimization process compared to other more general scatterers, such as those designed with topology optimization or even freeform wires. For example, for more general freeform wires, one needs to apply complicated constraints to avoid the object overlapping with itself. Similar difficulties appear with more general structures with an optimized topology. There, incorporating constraints that reflect the limitations of a given fabrication technology chosen for the implementation remains an important challenge. Concerning the use of silver, the previously reported helix[20] with a high em-chirality value at an infrared wavelength of $\lambda_0 = 200$ $\mu$m was made from silver. Moreover, silver has been reported to be a very suitable material to make artificial nanophotonic scatterers out of it that support strong magnetic resonances.[29] Combined with the higher plasma frequency and the lower damping compared to other noble metals such as gold or aluminum, silver was identified as the best candidate to consider in our quest to identify high em-chiral helices up to optical frequencies.

To identify silver helices with high $\overline{\chi}$ values for different illumination wavelengths, we combined numerical techniques to compute the em-chirality of complex geometries and also their shape derivatives with a machine learning algorithm for global optimization. We run different optimizations covering a wavelength range from 150 $\mu$m down to 500 nm to explore the frequency dependency of $\overline{\chi}$ for optimal helices as well as their geometrical properties. Promising designs were realized through nanofabrication, and their optical response was experimentally characterized. The optical response of the optimal design and that of the fabricated sample showed discrepancies. Nevertheless, a refined analysis considering both the deviating geometry of the helices, as extracted from SEM images, and material properties accommodating oxidation of silver, clearly explained the difference. The results made it possible to numerically assess the suitability of the designed and fabricated samples in helicity filtering glasses. We demonstrate that, at the operational wavelength of 3 $\mu$m, a 6.5 $\mu$m slab of randomly arranged helices at 0.5% filling factor can absorb 99% of the light of unwanted helicity while absorbing only 10% of the light of the desired helicity. For the same rejection of the unwanted helicity, both the optimal design at 800 nm and the fabricated helices would need slabs of 4.6 and 15 $\mu$m, respectively, which would absorb 50% and 85% of the desired light, respectively. Our results indicate that theoretical and fabrication improvements are needed to extend the performance of infrared helices onto the optical band.

This work is structured in three parts. First, we show the optimization results and we then analyze the response of different helices obtained during the numerical optimization process. Second, after obtaining the optimal designs, we analyze the response of experimentally realized helices for one of the optimal designs obtained at optical frequencies. Third, we use a simple homogenization theory model to analyze the performance of some of the designs obtained for creating an omni-angle circular polarization filter.

## ■ OPTIMIZATION RESULTS

The normalized em-chirality, $\overline{\chi}$, of an object is defined[20] based on the T-matrix of the object (e.g., ref 30, Chapter 5) using a basis of elementary fields of pure helicity, for example multipoles.

The T-matrix, **T**, gives the field scattered by the object upon illumination with any field. It maps a vector containing the illumination coefficients, used to expand a given illumination into the fields of the illumination basis set, to a vector of scattering coefficients,

$$\mathbf{E}_{\mathrm{scat}} = \mathbf{T}\mathbf{E}_{\mathrm{illu}} \tag{1}$$

In the Methods section, we provide a more detailed description of the T-matrix and the multipoles of a well-defined helicity.

Using the T-matrix, one can compute $\overline{\chi}$ as follows:[20]

$$\overline{\chi} = \frac{\left\| \begin{bmatrix} \mathrm{svd}(\mathbf{T}^{+,+}) \\ \mathrm{svd}(\mathbf{T}^{-,+}) \end{bmatrix} - \begin{bmatrix} \mathrm{svd}(\mathbf{T}^{-,-}) \\ \mathrm{svd}(\mathbf{T}^{+,-}) \end{bmatrix} \right\|}{\|\mathbf{T}\|} \tag{2}$$

where svd $(\mathbf{A})$ denotes a vector containing the singular values of matrix **A**, $\|\mathbf{A}\|$ denotes the Frobenius norm of matrix **A**, and $\mathbf{T}^{\pm,\pm}$ are the submatrices of the T-matrix for specific helicities of the illumination and scattered fields. The brackets indicate vectors obtained by stacking vertically the vectors of singular values.

The length and values of the svd-vectors change with the size of the T-matrix, or equivalently, with the maximum multipolar order used to expand the illumination and scattered fields. One needs to take into account the multipoles until a high enough multipolar order such that the extra entries of **T** are negligible, or, in other words, until the values of the main singular values and therefore of $\overline{\chi}$ have converged.

We use the finite element method solver JCMsuite to numerically calculate the T-matrices of the helices.[31,32] Besides calculating the T-matrix, we exploit the calculation of shape derivatives[33−35] of the T-matrix based on the forward method.[36,37] This technique generates, within the same finite element simulation, both the em-chirality of the object and its shape derivatives with respect to the geometrical parameters of the helix. To the best of our knowledge, this is the first time that a method to calculate shape derivatives of T-matrices for generally complex scatterers is presented and used for optimization. The method can be used in the design of scatterers for many applications that rely on a multipole description of the scatterer response.[38−42] The capability of computing shape derivatives of a multipole decomposition is not limited only to the FEM, but it could be potentially done with a wide variety of other numerical methods that can be used to compute T-matrices such as, for example, the extended boundary condition method.[43,44] Up to our knowledge, the shape derivatives have also been computed with the surface integral method[45] or for spheres[46] by differentiating the Mie coefficients. Once computed, the shape derivatives can also be used in the superposition T-matrix method (STMM) to obtain derivatives in multiscattering problems.[46] The details of the FEM simulations and how we compute the T-matrices and their shape derivatives are presented in Methods.

Four parameters describe the geometry of the helices: the radius of the helix spine, $R_h$, the thickness of the helix wire, $T_w$, the pitch of the helix, $P_h$, and the number of turns, $N_{turns}$. To optimize the different helices, we combine the finite element method to calculate the em-chirality with a Bayesian optimization based on Gaussian processes[47,48] as the optimization algorithm. This algorithm was shown to be an efficient global optimization method for medium dimensional optimization problems with expensive objective functions.[49] Furthermore, Bayesian optimization can incorporate derivative information on the objective function in a simple and elegant way (e.g., refs 50, Chapter 9.4, 51, and 52). The extra information provided by the shape derivatives can improve the optimization convergence rate. We provide the derivatives of the four parameters of the design space to the Gaussian process.

The optimizations are performed for different specific design vacuum wavelengths, $\lambda_d$, ranging from $\lambda_d = 150\ \mu$m to $\lambda_d = 500$ nm. Our goal is to see whether we can obtain helices with large $\overline{\chi}$ values along the entire infrared spectrum and also at optical wavelengths. In case this is not possible, we aim to study at which spectral region the material properties of the silver do not allow helices with large em-chirality to be obtained. That breakdown of the functionality is expected to happen toward optical wavelengths. In this spectral region, silver tends to be a poor metal due to the onset of absorption. Also, silver is no longer metallic above the plasma frequency, and it would not sustain localized plasmon polaritons that are key for a resonant light−matter interaction in metals. The permittivity for silver at each wavelength is interpolated from two databases[53,54] depending on the frequency range.

We start the optimization at long wavelengths because of the availability of designs that already work quite well.[20] These known designs allow for a rough estimation of the parameter space within which an optimization is feasible.

In total, we performed 12 optimization runs, each one corresponding to a different design wavelength of interest. Each run took between one and two days, during which we evaluated 500 different points of the design space. Those points are chosen by the Bayesian optimization algorithm. Methods section presents further details of the optimization process.

The results of the optimizations are shown in Figures 1 and 2. The optimal em-chirality values found for the different wavelengths are shown in Figure 1. Figure 2 shows the corresponding parameters of the optimal helices. As we can see in Figure 1, we found helices with $\overline{\chi}$ values larger than 0.9 at wavelengths down to 3 $\mu$m. Below this wavelength, $\overline{\chi}$ starts to drop, and at 500 nm, we could not find helices with values higher than 0.58.

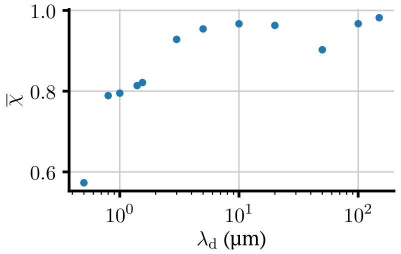

**Figure 1.** Electromagnetic chirality of silver helices with optimized geometrical parameters at different design wavelengths, $\lambda_d$. Each point shows the normalized em-chirality value, $\overline{\chi}$, of the optimal helix found for that specific operational wavelength.

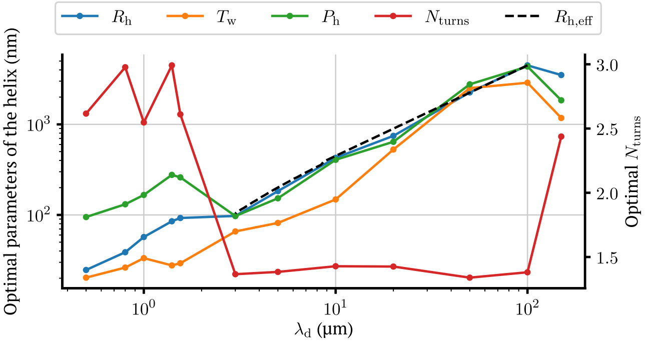

**Figure 2.** Geometrical parameters of each optimal helix obtained at each design wavelength $\lambda_d$. The parameters defining the shape of the helix are the radius of its spine, $R_h$, the thickness of the helix wire, $T_w$, the pitch per turn of the helix, $P_h$, and the total winding number, $N_{turns}$. $R_{h,eff}$ shows the downscaling of the value of $R_h$ with the wavelength, $\lambda_d$, calculated with a scaling design rule for plasmonic materials.[55]

Inspecting both Figure 1 and Figure 2, one can distinguish two wavelength regions with different behaviors. The optimal designs found at wavelengths above $\lambda_d = 3\ \mu$m present a similar shape. In this region, the optimal helices have a similar number of turns, and also the ratio between the radius of the helix spine $R_h$ and the pitch of the helix keeps more or less constant. Moreover, these last two parameters seem to scale linearly with the operational wavelength. All these observations can be explained based on the approximation of the material properties of silver in this wavelength region as a perfect electric conductor. The black dashed line plotted in Figure 2 represents the downscaling of the optimal helix obtained at $\lambda_d$

= 100 $\mu$m following the design scaling rule for plasmonic materials described in ref 55. This scaling factor differs slightly from unity only in the region between 3 and 10 $\mu$m. Some small deviations from this scaling rule present in the optimization results could be explained by the fact that the FEM simulations take into account the effects of a nonzero thickness of the wire. Even in cases where it is much smaller than the wavelength, this can play an important role in the scattering response.[56]

For wavelengths closer to the optical region, the conductivity of silver diminishes. Thus, it will be increasingly complicated for the helix to sustain a suitable balance between electric and magnetic dipolar resonance necessary to obtain large values for the em-chirality.[57−59] The decrease can also be rationally appreciated from considering the limiting behavior. Halving the size of the helix at far-infrared frequencies allows doubling the operational frequency. However, the possibility of silver to sustain localized plasmon polaritons is bound to a lower wavelength of approximately 360 nm due to the underlying material dispersion. Therefore, halving the size does not allow to halve the operational wavelength when approaching the visible part of the spectrum. Instead, the resonance wavelength is adiabatically pushed toward the lower bound. This implies a decreasing ratio of the absolute size of the helix to the operational wavelength. In turn, this suggests that the resonance strength decreases. In particular, the magnetic dipolar response can only be weakly excited for a decreasing size of the object. This effect lowers the achievable magnetic response required for large em-chirality values. Similar effects have been encountered when studying the scaling behavior of, for example, split-ring resonators.[29,60,61]

To analyze the properties of the optimal helices, we take as an example the helix optimized for an illumination wavelength of 3 $\mu$m. In Figure 3, we plot its em-chirality and scattering cross-section as a function of the wavelength. We see that the maximum em-chirality corresponds to a peak of the rotationally averaged scattering cross-section. This maximum implies that it is not an undesirable optimum where the em-chirality is high and the interaction strength is low, but rather that it is a resonance. Figure 3 also shows 2 orders of magnitude differences in the energy scattered by the helix for illumination fields of different helicities. We notice that an object so close to the maximal possible em-chirality barely interacts with light of one helicity while interacting strongly with the opposite helicity. Such a response is in stark contrast to an achiral object that interacts identically with light of both helicities.

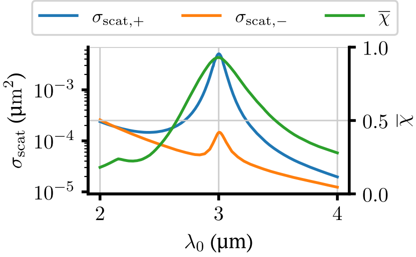

**Figure 3.** Spectral dependency of the em-chirality and the rotational averaged scattering cross-section $\sigma_{\text{scat}}$ for the helix optimized for an operational wavelength of $\lambda_{\text{d}} = 3$ $\mu$m (100 THz). The scattering cross-section is split into the values of the interaction with fields of both helicities.

This difference in the interaction with fields of different helicities is also visible in Figure 4. The figure shows the intensities of the scattering near-fields close to the helix upon illumination with a plane wave propagating in the $x$-direction. The plane wave is circularly polarized, either left- or right-handed. The intensity of the near-field is approximately 2 orders of magnitude higher for the right circularly polarized plane wave illumination.

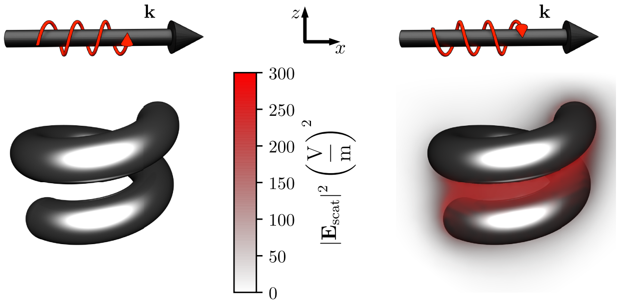

**Figure 4.** Scattered near-field intensity obtained when the optimized helix for an operational wavelength of 3 $\mu$m is illuminated with two plane waves of different circular polarizations and the same wavelength and direction. The plane waves have a vacuum wavelength of 3 $\mu$m, and their wave vector is parallel to the $x$-axis. The electric field strength of the plane waves is 1 V/m. The left and right figures show the fields for the left and right circular polarizations, respectively.

Figure 5 shows the absorption cross-section for the different directions of illuminating plane waves and both circular polarizations. We see how the largest difference between polarizations arises for plane waves perpendicular to the axis of the helix, as the one used the calculate the near-field in Figure 4. For this direction, the absorption is 2 orders of magnitude larger for right circularly polarized light. The large differences in the scattering and absorption cross sections provided by this helix for different illumination directions render it a good candidate to be used in a direction-independent circular polarization filter, as proposed in ref 20.

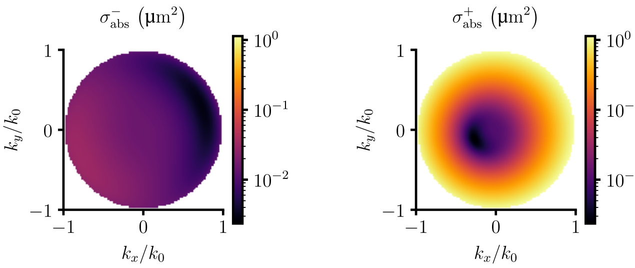

**Figure 5.** Absorption cross sections, $\sigma_{\text{abs}}$, of the helix optimized for an operational wavelength of 3 $\mu$m when it is illuminated with plane waves of different circular polarizations. The plot shows $\sigma_{\text{abs}}$ as a function of the direction of the plane waves, represented in k-space. The helix winds around the $z$-axis.

## EXPERIMENTAL RESULTS

In a further step, we fabricated the optimal helix obtained for the design wavelength of 800 nm and measured its optical response. The helices are fabricated with a vapor deposition technique described in the Methods section. They are made with 95% silver and 5% copper in their composition. Because

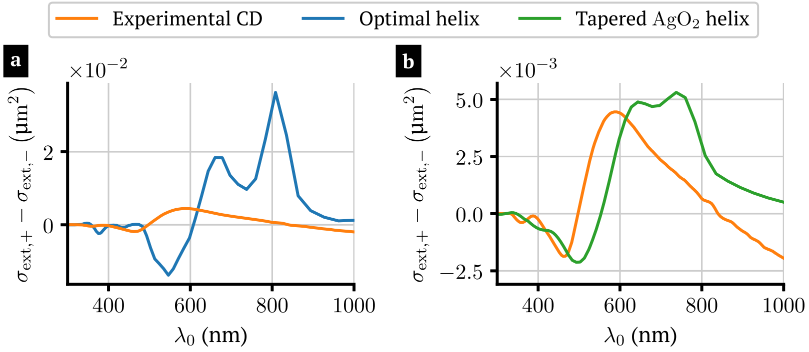

**Figure 6.** (a) Experimental rotationally averaged differential extinction cross sections $\sigma_{\text{ext},+} - \sigma_{\text{ext},}$ with respect to the vacuum illumination wavelength, $\lambda_0$, for the fabricated helices (orange) and the numerical values for the optimized helix (blue). The values of the experimental results are obtained from the experimental CD signal, in millidegrees, based on the concentration of helices into the solvent. The details of the conversion are explained in Methods. (b) The orange line shows the same results as in (a). The green line shows the numerical results of the differential extinction cross-section for a partially oxidized tapered helix. The shape of the helix is shown in Figure 7c.

the CD measurement is performed with helices immersed into Milli-Q water, the helix geometry is optimized again to maximize $\bar{\chi}$ under the conditions of the experimental setup. The chirality of this new design reaches a value of 0.76 at the design wavelength. The parameters of the optimal helix are indicated in the caption of Figure 7. The blue line in Figure 6a shows the numerical CD spectrum of the new design. The orange lines of Figure 6 show the CD signal from the experimental measurement. One can observe how both CD spectra differ considerably in magnitude and dispersion.

To find a reason for the discrepancy, we look at SEM images of the fabricated helices before their release from the substrate into solution in Figure 7a. From the image one can notice that the fabricated helices differ from the optimal design, Figure 7b, mainly in the pitch. Also, some of the fabricated helices appear to be slightly tilted and feature a tapered shape. We stress that the fabrication is challenging. To test if the difference in geometry was the source of the discrepancy between the predicted and obtained measurements, we generated a CAD model of a helix that better resembles the shapes appearing in the SEM image. The shape of this revised CAD model is shown in Figure 7c. However, the geometry adjustment did not provide a much better agreement between the experimental and numerical results.

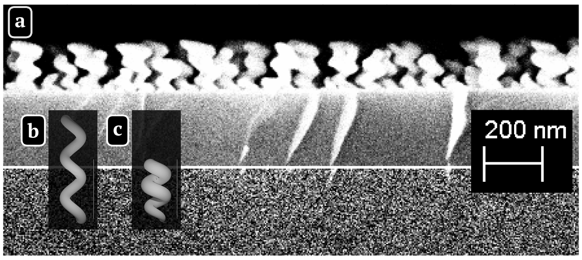

**Figure 7.** (a) SEM image of the fabricated helices. The helices were fabricated using a vapor deposition technique described in the Methods section. (b) Rendered image of the helix that came as a result of the numerical optimization process. Its parameters are $R_h$ = 27.4 nm, $T_h$ = 35 nm, $P_h$ = 137 nm, and $N_{\text{turns}}$ = 2.4. Its helicity differential extinction cross-section corresponds to the blue line of Figure 6a. (c) Rendered image of the CAD model of a tapered helix used for trying to reproduce the experimental results numerically. The green line shows its helicity differential extinction cross-section signature in Figure 6b. All images a, b, and c present the same scale and, therefore, can be directly compared.

The improved agreement appeared when we took into consideration a likely oxidation process of the helices. To check this hypothesis, we calculated new values for the silver permittivity of the helix as a weighted sum with 70% silver[53] and 30% partially oxidated silver. The permittivity values of the silver oxide were extracted from Figure 1 of ref 62 using the plot line for the lower flux of oxygen. The new numerical results obtained, also using the CAD model of Figure 7c, are shown in Figure 6b. One can see a much better agreement between the experimental and these newly computed results. The maximum $\bar{\chi}$ value obtained with these new calculations is 0.27. Nevertheless, one can still appreciate a wavelength shift between both results. We assume that this difference might be due to the material properties of the helices because reasonable modifications of the geometry parameters of the CAD model, in agreement with the observed differences in the SEM image, did not shift the peaks of the resonances significantly.

Repeating the optimization process, taking into consideration the oxidation of silver, we obtained an optimal $\bar{\chi}$ value of 0.49 instead of 0.76. The results of this additional optimization are presented in the Supporting Information. Additionally, one can find a calculation of how $\bar{\chi}$ deviates from the optimal value when the helix deviates from its optimal shape toward the shape shown in Figure 7c.

The experimental results indicate that the fabrication of optimal helices at optical frequencies is a fabrication challenge that may be tackled for the fabrication technique used here and for other techniques.[63,64]

## ■ BROAD-ANGLE FILTER

To give an estimate of the implications of different values of the em-chirality $\bar{\chi}$ of a scattering object, we now look at the performance of some of the analyzed helices when used to create an omni-angle polarization filter. In this comparison, we consider the optimal helix embedded in a vacuum obtained for a design wavelength of $\lambda_d$ = 3 $\mu$m, the optimal helix obtained for a design wavelength of $\lambda_d$ = 800 nm and embedded in water, and the tapered helix obtained as a result of trying to match the experimental and the numerical results. To make this comparison, we use a rather simple approximation of the filter. We will assume that the filter, composed of randomly oriented helices embedded in a homogeneous medium with

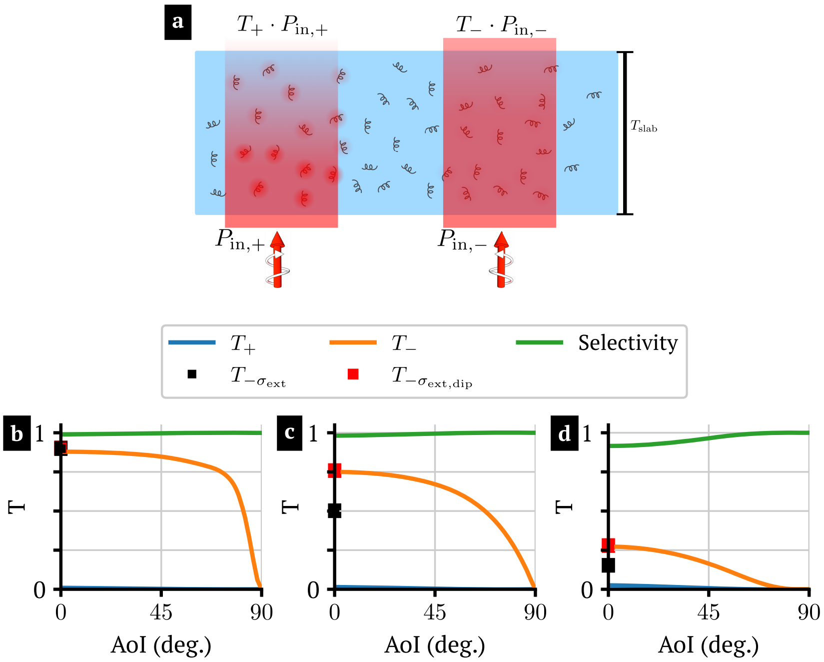

**Figure 8.** (a) Sketch of the omni-directional polarization filter concept. The filter consists of an embedding medium containing randomly positioned and oriented silver helices with the same winding direction. (b−d) Performance of three different polarization filters. The lines show the transmittance of the filters depending on the angle of incidence of the illumination beam for beams with both helicities. The transmittance had been calculated using a transfer matrix approach that considers effective material properties extracted from the dipolar part of the T-matrices. The black squares show the transmittance at normal incidence computed using the extinction cross-section obtained from the full T-matrices of the helices. The red squares show the same quantity when using T-matrices containing only the dipole terms. (b) Filter made out of helices with the design obtained from the optimization at $\lambda_d = 3$ $\mu$m. The performance of the filter is measured at a vacuum wavelength $\lambda_0$ of 3 $\mu$m. (c) Filter made out of helices obtained from the optimization result at the design wavelength $\lambda_d = 800$ nm. The performance of the filter is measured at a vacuum wavelength $\lambda_0$ of 800 nm. (d) Filter made out of the silver oxidized helices model shown in the previous section. The performance of the filter is measured at a vacuum wavelength $\lambda_0$ of 740 nm. From left to right, the filters have thicknesses of 6.5, 4.6, and 15.2 $\mu$m, respectively. The selectivity is calculated as $(T - T_+)/(T + T_+)$.

the refractive index of either vacuum or water, can be treated as a single homogenized material. The power loss experienced by a circularly polarized beam propagating along this material in the forward direction can be expressed through the rotationally averaged helicity extinction cross sections for the respective polarization[58,65] of the helices, $\sigma_{\text{ext},\pm}$. If we consider a slab of this homogenized material with a thickness $\Delta z$, assuming that it is thin enough for the power flux of the incident beam remaining approximately constant, the power per unit area absorbed or scattered by the medium with a helix number density $\rho_{\text{helices}}$ can be obtained as

$$S_z(z + \Delta z) - S_z(z) = -\Delta z \rho_{\text{helices}} S_z(z) \sigma_{\text{ext},\pm} \tag{3}$$

with $S_z$ being the component of the time averaged Poynting vector along the propagation direction of the beam. In the limit $\Delta z \to 0$, one obtains that the change of the power flux along the propagation direction of the beam equals,

$$\frac{dS_z(z)}{dz} = -S_z(z)\rho_{\text{helices}}\sigma_{\text{ext},\pm} \tag{4}$$

which gives us the value of the power flux of the beam as a function of the initial power flux, $S_{z,0}$, before entering the slab of homogenized material

$$S_z(z) = S_{z,0} e^{-\rho_{\text{helices}}\sigma_{\text{ext},\pm} z} \tag{5}$$

To compare how the filters would absorb beams of different helicity, we set the thickness of the homogenized slab such that it absorbs 99% of the incoming power for the beam with helicity +1. We will use a helix volume filling fraction of 0.5%. We are confident that, for this filling fraction, the chosen homogenization model can give a good estimation of the transmittance.[66,67] The thickness turns out to be a slab of 6.5 $\mu$m for the material composed of optimal helices for the design wavelength of 3 $\mu$m, 4.6 $\mu$m for the material composed of optimal helices obtained for the design wavelength of 800 nm, and 15.2 $\mu$m for a material composed of the tapered silver oxidized helices. The results for the performance of the three filters, obtained with this simple model, are shown in Figure 8 by the black squares. We only included the results for the beams with helicity −1 for clarity reasons. For this case, the slab with the helices designed at $\lambda_d = 3$ $\mu$m lets 90% of the incoming power flux through, the slab with helices designed at $\lambda_d = 800$ nm transmits 50%, and the slab composed of the tapered silver oxidized helices transmits 15% of the incoming power flux.

Additionally, we analyzed the transmittance of the filter using a second methodology. We retrieved the effective material parameters of the slab from the polarizabilities of the helices,[68] which were obtained directly from the computed T-matrices.[58] These effective material parameters are the permittivity, $\epsilon_{\text{eff}}$, permeability, $\mu_{\text{eff}}$, and chirality parameter, $\kappa_{\text{eff}}$. Once obtained, we compute the transmittance of the slab using a transfer matrix method with the Fresnel coefficients generalized to chiral media.[69] This second method allows the analysis of the transmittance as a function of the angle of incidence (AoI) of the beams.

The results are shown by the solid lines in Figure 8b−d for the three helices, respectively. As one can see, the results at normal incidence, that is, where the AoI equals 0°, are in good agreement but do not perfectly match the ones obtained using the previous model. The respective values are indicated with black squares in Figure 8. We hypothesize that the main reason for the slight remaining deviation could be linked to the fact that the second model, that is, the effective medium description, is based on the dipolar polarizabilities. In essence, it neglects the presence of higher-order multipoles in the response of the helices. If the contribution of these higher-order multipoles is not negligible for these two helices, the model will underestimate the power losses through the propagation of the beam.

To verify this hypothesis, we again computed the transmittance at normal incidence using the first model, that is, based on the extinction cross sections. But this time, the extinction cross-section was computed only from the dipolar contributions to the T-matrices. The results are shown in Figure 8 by the red squares. As we can see, the results obtained from the first and the second model coincide perfectly when only the dipole terms are taken into account for computing $\sigma_{\text{ext},\pm}$. This result indicates that the performance shown by the transmittance curves in Figure 8c,d is slightly overestimated when using the retrieved effective parameters.

Looking now into the performance of the filters with respect to the angle of incidence, we can see that the performance of the filters does not drop significantly until angles higher than 60°. Therefore, the concept allows for filters with a wide field of view.

From right to left, Figure 8 shows the performance of a device that can be currently fabricated, one device that could be obtained if one could further improve the fabrication process, and one that, for achieving a similar behavior at optical frequencies, further theoretical work needs to be done to obtain a suitable design.

## CONCLUSION

We have optimized silver helices for maximizing their electromagnetic chirality at particular frequencies ranging from the far-infrared to the optical band. Values larger than 90% of the maximum possible value have been obtained from the lowest frequency up to a wavelength of 3 $\mu$m. As the frequency increases into the optical band, the electromagnetic chirality of the helices decreases monotonically to just below 0.6 at 500 nm.

For the optimization, we have combined a method for computing shape derivatives for T-matrices of complex structures with a Bayesian optimization algorithm that supports the use of derivative information.

In accordance with their high electromagnetic chirality, the optimized helices show a strong difference in the interaction with fields of different handedness, including the rotationally averaged differential interaction and absorption cross sections. These differences make them suitable components in devices for different applications such as helicity filtering glasses. We demonstrate that, at the operational wavelength of 3 $\mu$m, an 8 $\mu$m slab of randomly arranged helices at 0.5% filling factor can absorb 99% of the light of unwanted helicity while absorbing only 10% of the light of the desired helicity.

Further theoretical research is necessary to find different materials and designs that enable a similar behavior deep in the optical regime and possibly across an extended spectral domain. A basis for the application of a wide variety of mathematical optimization techniques has been provided by integrating em-chirality with mathematical formulations of scattering theory.[70] This, in principle, opens up the possibility of applying general free-form shape optimization techniques to the design problem. A first but already very promising option is to extend the shapes of the design space from helices to more complex free-form wires.[71,72]

Moreover, our experimental results for a design at 800 nm show that the performance of these structures strongly depends on an accurate realization of their optimal material properties and optimal shapes, with features as small as a few tens of nanometers.

Unlocking the applications of high em-chiral objects at optical frequencies hence implies addressing both theoretical and fabrication challenges.

## METHODS

**T-Matrix in the Helicity Basis.** The T-matrix of an object gives the scattering field produced by that object upon illumination with any given field. More precisely, the T-matrix is a matrix that maps a vector of illumination coefficients, corresponding to the expansion of the illumination into a basis set of elementary illumination fields, to the vector of scattering coefficients, corresponding to the expansion of the scattering field into a basis set of elementary scattering fields.

One of the most used basis sets for expanding the illumination and scattering fields are those of the regular and radiative vector spherical wave functions, or multipoles, respectively.

These sets of regular, $\mathbf{G}_{l,m}^{\pm,\text{reg}}(\mathbf{r})$, and radiative, $\mathbf{G}_{l,m}^{\pm,\text{rad}}(\mathbf{r})$, multipoles can be used to expand illumination and scattering fields, respectively:

$$\mathbf{E}_{\text{illu}}(\mathbf{r}) = \sum_{l=1}^{\infty} \sum_{m=-l}^{+l} a_{l,m}^{+}\mathbf{G}_{l,m}^{+,\text{reg}}(\mathbf{r}) + a_{l,m}^{-}\mathbf{G}_{l,m}^{-,\text{reg}}(\mathbf{r}) \tag{6}$$

$$\mathbf{E}_{\text{scat}}(\mathbf{r}) = \sum_{l=1}^{\infty} \sum_{m=-l}^{+l} b_{l,m}^{+}\mathbf{G}_{l,m}^{+,\text{rad}}(\mathbf{r}) + b_{l,m}^{-}\mathbf{G}_{l,m}^{-,\text{rad}}(\mathbf{r}) \tag{7}$$

where the plus and minus sign superscripts denote the multipoles of plus and minus helicity, respectively, $l$ denotes the multipolar order, and $m$ denotes the angular momentum along the $z$ direction. These multipoles of pure helicity can be obtained as a linear combination (ref 73, section 2.2.3) of the better known electric and magnetic multipoles:

$$\mathbf{G}_{l,m}^{+,(\text{reg},\text{rad})}(\mathbf{r}) = \frac{1}{\sqrt{2}}(\mathbf{N}_{l,m}^{(\text{reg},\text{rad})}(\mathbf{r}) + \mathbf{M}_{l,m}^{(\text{reg},\text{rad})}(\mathbf{r})) \tag{8}$$

$$\mathbf{G}_{l,m}^{-,(\text{reg},\text{rad})}(\mathbf{r}) = \frac{1}{\sqrt{2}}(\mathbf{N}_{l,m}^{(\text{reg},\text{rad})}(\mathbf{r}) - \mathbf{M}_{l,m}^{(\text{reg},\text{rad})}(\mathbf{r})) \tag{9}$$

where $\mathbf{N}_{l,m}^{(\text{reg},\text{rad})}(\mathbf{r})$ and $\mathbf{M}_{l,m}^{(\text{reg},\text{rad})}(\mathbf{r})$ are the electric and magnetic multipoles, respectively. In this work, we use the electric and magnetic multipoles as defined in the Appendix of ref 30.

Although, in principle, the expansions contain an infinite number of multipoles, for the practical study of light−matter interaction involving finite objects, it is possible to retain only the multipoles up to a certain maximum multipole order, $l_{\max}$.

Once the basis sets are given, the fields can then be completely determined by the expansion coefficients, $\mathbf{E}_{\text{illu}} =$

$[a^{+}_{1,-1}, ..., a^{+}_{l_{\max},+l_{\max}}, a^{-}_{1,-1}, ..., a^{-}_{l_{\max},+l_{\max}}]^{T}$. An equivalent expression applies for the scattered field.

For a given illumination $\mathbf{E}_{\text{illu}}$, the T-matrix of an object, $\mathbf{T}$, provides the field scattered by the object upon the illumination,

$$\mathbf{E}_{\text{scat}} = \mathbf{T}\mathbf{E}_{\text{illu}} = \begin{bmatrix} \mathbf{T}^{+,+} & \mathbf{T}^{+,-} \\ \mathbf{T}^{-,+} & \mathbf{T}^{-,-} \end{bmatrix} \mathbf{E}_{\text{illu}} \tag{10}$$

where we denote by $\mathbf{T}^{\pm,\pm}$ the submatrices of the T-matrix for specific helicities of the illumination and scattered fields.

**T-Matrix Calculation.** The T-matrices of the silver helices are computed using the finite element solver JCMsuite.[31,32] They are computed by illuminating the helix with a set of regular vector spherical wave functions, and the scattered fields produced by each illumination are expanded into a set of radiative vector spherical wave functions. The procedure is the same as described in ref 74. The only difference lies in the numerical method we use to expand the scattered fields, and which in our case is the one that we previously presented in ref 75. We use finite elements with a polynomial degree of 2. We need small mesh elements to reproduce the surface of the helix accurately and therefore do not benefit from higher polynomial degrees. The accuracy requirements would already be fulfilled because of the small mesh size. The maximum mesh size used for the helix domain is $\lambda/0.3$ for the longer wavelengths and $\lambda/2$ for the optical and near-infrared wavelengths. Note that $\lambda$ refers to the wavelength within the helix, and the refractive index of silver at the longer wavelengths exceeds values of 300 in both the real and imaginary parts. In the air domain, we use a mesh size of $\lambda/15$. Before starting a new optimization at each wavelength, a convergence test is done to know if further mesh refinement is needed. The criterion is to have a mesh that achieves errors in $\bar{\chi}$ lower than one percent. Regarding the simulation time, the time required to evaluate the em-chirality, $\bar{\chi}$, at each point of the design space depended on the specific design wavelength and specific size of each helix. On average, each finite element simulation took around 6 min. The additional time required to calculate $\bar{\chi}$, once computed the T-matrix with the FEM, is negligible.

**Calculation of the Derivatives of the T-Matrices Concerning the Geometrical Parameters of the Helix.** The shape derivatives are computed in a multistep process. Once a tetrahedralization of the helix is computed, a separate python script is used to read the mesh points that lie on the helix surface and subsequently obtain the parameters, $\theta_{\text{h}}$ and $\phi_{\text{h}}$, of the analytic parametrization of the helix corresponding to those points. Once the set of parameters is obtained, the derivatives are computed applying the chain rule to the parametrization. The derivatives of these mesh points are then passed back to JCMsuite, which finalizes the process of propagating the shape derivatives to the calculation of the T-matrix using the forward method.[33,36,37] The analytical expressions used for parametrizing the helix and its derivatives are shown in the Supporting Information.

**Optimization Process.** The optimization of the helices consisted of different optimization runs, each for the optimization of a helix at a different design wavelength, $\lambda_{\text{d}}$.

The optimization algorithm used in each optimization run was Bayesian optimization, more specifically, we used the optimization tool included in the software JCMsuite. This is just for our convenience, and one could use other available Bayesian optimization packages.[76−79] After each new FEM simulation was computed, we included the value of the calculated $\bar{\chi}$ plus its derivatives with respect to the four design parameters: $R_{\text{h}}$, $T_{\text{w}}$, $P_{\text{h}}$, and $N_{\text{turns}}$ into the Gaussian process of the optimization algorithm.

The limits of the parameter space for the different optimization runs were set downscaling the ones used in the first optimization run for $\lambda_{\text{d}} = 150$ $\mu$m. At the illumination wavelength of 150 $\mu$m, the lower and upper limits for the radius of the helix, $R_{\text{h}}$, were set to 1 and 10 $\mu$m, respectively. When we decreased the operational wavelength, they were accordingly linearly scaled down. The thickness of the wire, $T_{\text{w}}$, was allowed to vary between 5% and 95% of the value of the radius of the helix. An additional lower limit was imposed on the thickness of the wire. It could not be smaller than 20 nm for any of the simulations, independently of the wavelength. This reflected fabrication limits in making extremely thin wires. It also accommodated the lower bound for the critical dimension of the radius of the wire to rely on macroscopic Maxwell's equations equipped with bulk constitutive relations to describe the light−matter interaction (e.g., ref 80, section 6.6). The pitch of the helix, $P_{\text{h}}$, was set relative to the thickness of the wire. It could vary between 1.1 and 10 times the thickness. The limits for the number of turns were 0.1 and 4. However, none of the optimal designs lay on the boundaries set by the optimization constraints. Even for the shorter wavelengths, where one could expect that the optimal shape could possibly lay on the thickness limit of 20 nm, the optimal helices were found out of the constraint boundaries. We show in the Supporting Information the sampling of the parameter space carried during the optimization process for some of the design wavelengths.

Each optimization run consisted of 500 finite element simulations of different helices of the design space. The parameters to be simulated were chosen by the Bayesian optimization algorithm. After the 500 simulations, the optimization process would continue if the value of the expected improvement,[81,82] obtained from the Gaussian process, would be higher than $10^{-12}$. However, this was not the case for any of the optimization runs, and all of them stopped after the 500 iterations.

**Experimental Realization of the Helices.** Dedicated helices were fabricated by a published shadow growth physical vapor deposition technique that combines glancing angle deposition (GLAD) with nanopatterning (nanoGLAD).[83] Briefly, a silicon wafer was cleaned and then prepatterned with a monolayer of hexagonally arranged gold nanoparticles using Block Copolymer-Micelle-Lithography (BCML).[84] Silver (Ag) and copper (Cu) were then heated by an electron beam and deposited onto the patterned wafer under high vacuum. The angle between the flux direction of the incident atoms and the substrate normal was $\alpha = 87°$. The gold nanoparticles facilitate shadowing and act as seeds for the subsequent growth. The spacing between the seeds was $d = 76$ nm. During the deposition process, the substrate was cooled with liquid nitrogen and slowly rotated about the substrate normal, leading to the formation of helically shaped $\text{Ag}_{0.95}\text{Cu}_{0.05}$ nanostructures with 2.4 turns. After the fabrication was completed, the particles were removed from the substrate and transferred into (Milli-Q) water via ultrasonication. The geometric helix dimensions were extracted from scanning electron micrographs (pitch $P_{\text{h}} = 72.5 \pm 3.5$ nm, wire width $T_{\text{w}} = 44.1 \pm 6.6$ nm, radius $R_{\text{h}} = 23.5 \pm 6.7$ nm), an example image of the fabricated helices is presented in Figure 7a. The sonicated wafer piece had an area of $A_w \approx 25 \times 10^{-6}$ m$^2$. We thus estimate that the colloidal suspension contains

$$N_p = \frac{2A_w}{\sqrt{3}\,d^2} = 5 \times 10^9 \tag{11}$$

particles. The particles have been suspended in 1.7 mL of water. Hence, the number density of the colloidal solution containing the helices was $N = 2.9 \times 10^{15}$ m$^{-3}$. However, it is important to realize that this value only reflects an upper bound. In practice, imperfections in the seed layer or during the fabrication result in fewer particles on the wafer. We thus estimate a number density for the colloidal solution of $N = (1.6 \pm 1.3) \times 10^{15}$ m$^{-3}$.

## ■ ASSOCIATED CONTENT

### ● Supporting Information

The Supporting Information is available free of charge at https://pubs.acs.org/doi/10.1021/acsphotonics.1c01887.

> Multipole decomposition of the CD spectrum for the optimal helix at $\lambda_d$ = 800 nm. Calculation of the normalized em-chirality for geometry variations with respect to the optimal design at $\lambda_d$ = 800 nm. Detailed results of the optimization process for some selected design wavelengths. Results of the optimization process for a partially oxidized silver helix. Expressions for the parametrization of the helix and its shape derivatives (PDF)

## ■ AUTHOR INFORMATION

### Corresponding Author

**X. Garcia-Santiago** − *Institute of Nanotechnology, Karlsruhe Institute of Technology, 76021 Karlsruhe, Germany;* orcid.org/0000-0002-8958-4967; Email: xavier.garcia-santiago@kit.edu

### Authors

**M. Hammerschmidt** − *JCMwave GmbH, 14050 Berlin, Germany; Computational Nano Optics, Zuse Institute Berlin, 14195 Berlin, Germany*

**J. Sachs** − *Max Planck Institute for Intelligent Systems, 70569 Stuttgart, Germany*

**S. Burger** − *JCMwave GmbH, 14050 Berlin, Germany; Computational Nano Optics, Zuse Institute Berlin, 14195 Berlin, Germany;* orcid.org/0000-0002-3140-5380

**H. Kwon** − *Max Planck Institute for Intelligent Systems, 70569 Stuttgart, Germany;* orcid.org/0000-0002-5300-1002

**M. Knöller** − *Institute for Applied and Numerical Mathematics, Karlsruhe Institute of Technology, 76131 Karlsruhe, Germany*

**T. Arens** − *Institute for Applied and Numerical Mathematics, Karlsruhe Institute of Technology, 76131 Karlsruhe, Germany*

**P. Fischer** − *Max Planck Institute for Intelligent Systems, 70569 Stuttgart, Germany; Institute of Physical Chemistry, University of Stuttgart, 70049 Stuttgart, Germany;* orcid.org/0000-0002-8600-5958

**I. Fernandez-Corbaton** − *Institute of Nanotechnology, Karlsruhe Institute of Technology, 76021 Karlsruhe, Germany;* orcid.org/0000-0003-2834-5572

**C. Rockstuhl** − *Institute of Nanotechnology, Karlsruhe Institute of Technology, 76021 Karlsruhe, Germany; Institute of Theoretical Solid State Physics, Karlsruhe Institute of Technology, 76131 Karlsruhe, Germany; Max Planck School of Photonics, 07745 Jena, Germany*

Complete contact information is available at: https://pubs.acs.org/10.1021/acsphotonics.1c01887

### Funding

The authors gratefully acknowledge financial support by the Deutsche Forschungsgemeinschaft (DFG, German Research Foundation) through Project-ID 258734477 - SFB 1173 and Project-ID 390761711 - EXC 2082/1, from the European Union's Horizon 2020 research and innovation program under the Marie Sklodowska-Curie Grant Agreement No. 675745, by the Helmholtz Association via the Helmholtz program "Materials Systems Engineering" (MSE), and the KIT through the "Virtual Materials Design" (VIRTMAT) project. We acknowledge support from the Karlsruhe School of Optics and Photonics (KSOP) and from the Carl Zeiss Foundation via the CZF-Focus@HEiKA program. This project has received funding from the German Federal Ministry of Education and Research (BMBF Forschungscampus MODAL, Project Number 05M20ZBM) and from the Deutsche Forschungsgemeinschaft (Excellence center MATH+, EXC-2046/1, Project ID: 390685689).

### Notes

The authors declare no competing financial interest.

## ■ REFERENCES

(1) Kelvin, W. T. B. *The Molecular Tactics of a Crystal*; Clarendon Press, 1894.

(2) Mun, J.; Kim, M.; Yang, Y.; Badloe, T.; Ni, J.; Chen, Y.; Qiu, C.-W.; Rho, J. Electromagnetic chirality: from fundamentals to nontraditional chiroptical phenomena. *Light Sci. Appl.* **2020**, *9*, 1−18.

(3) Richardson, R. D.; Baud, M. G. J.; Weston, C. E.; Rzepa, H. S.; Kuimova, M. K.; Fuchter, M. J. Dual wavelength asymmetric photochemical synthesis with circularly polarized light. *Chem. Sci.* **2015**, *6*, 3853−3862.

(4) Yang, G.; Xu, Y. Y.; Zhang, Z. D.; Wang, L. H.; He, X. H.; Zhang, Q. J.; Hong, C. Y.; Zou, G. Circularly polarized light triggered enantioselective thiolene polymerization reaction. *Chem. Commun.* **2017**, *53*, 1735−1738.

(5) He, C.; Yang, G.; Kuai, Y.; Shan, S.; Yang, L.; Hu, J.; Zhang, D.; Zhang, Q.; Zou, G. Dissymmetry enhancement in enantioselective synthesis of helical polydiacetylene by application of superchiral light. *Nat. Commun.* **2018**, *9*, 1−8.

(6) Schäferling, M.; Dregely, D.; Hentschel, M.; Giessen, H. Tailoring enhanced optical chirality: design principles for chiral plasmonic nanostructures. *Phys. Rev. X* **2012**, *2*, 031010.

(7) Mohammadi, E.; Tsakmakidis, K. L.; Askarpour, A. N.; Dehkhoda, P.; Tavakoli, A.; Altug, H. Nanophotonic platforms for enhanced chiral sensing. *ACS Photonics* **2018**, *5*, 2669−2675.

(8) Hentschel, M.; Schäferling, M.; Duan, X.; Giessen, H.; Liu, N. Chiral plasmonics. *Sci. Adv.* **2017**, *3*, e1602735.

(9) Schäferling, M.; Yin, X.; Engheta, N.; Giessen, H. Helical plasmonic nanostructures as prototypical chiral near-field sources. *ACS Photonics* **2014**, *1*, 530−537.

(10) Jeong, H.-H.; Mark, A. G.; Alarcón-Correa, M.; Kim, I.; Oswald, P.; Lee, T.-C.; Fischer, P. Dispersion and shape engineered plasmonic nanosensors. *Nat. Commun.* **2016**, *7*, 1−7.

(11) Vestler, D.; Shishkin, I.; Gurvitz, E. A.; Nasir, M. E.; Ben-Moshe, A.; Slobozhanyuk, A. P.; Krasavin, A. V.; Levi-Belenkova, T.; Shalin, A. S.; Ginzburg, P.; Markovich, G.; Zayats, A. V. Circular dichroism enhancement in plasmonic nanorod metamaterials. *Opt. Express* **2018**, *26*, 17841−17848.

(12) Graf, F.; Feis, J.; Garcia-Santiago, X.; Wegener, M.; Rockstuhl, C.; Fernandez-Corbaton, I. Achiral, helicity preserving, and resonant

structures for enhanced sensing of chiral molecules. *ACS Photonics* **2019**, *6*, 482−491.

(13) Feis, J.; Beutel, D.; Köpfler, J.; Garcia-Santiago, X.; Rockstuhl, C.; Wegener, M.; Fernandez-Corbaton, I. Helicity-preserving optical cavity modes for enhanced sensing of chiral molecules. *Phys. Rev. Lett.* **2020**, *124*, 033201.

(14) Kelly, S. M.; Jess, T. J.; Price, N. C. How to study proteins by circular dichroism. *Biochim. Biophys. Acta* **2005**, *1751*, 119−139.

(15) Chadha, A. S.; Zhao, D.; Zhou, W. An all-dielectric broadband high-transmission efficiency circular polarizer. In *Photonic and Phononic Properties of Engineered Nanostructures IV*, Proceedings of the Spie Opto, San Francisco, CA, Feb 1−6, 2014, SPIE Press, Bellingham, WA, 2014; pp 145−152.

(16) Rangelov, A.; Droulias, S.; Yannopapas, V. A broadband optical isolator based on chiral plasmonic-metamaterial design. *Prog. Electromagn. Res. M* **2019**, *81*, 67−73.

(17) Fowler, P. W. Quantification of chirality: Attempting the impossible. *Symmetry: Cult. Sci.* **2005**, *16*, 321−334.

(18) Buda, A. B.; Mislow, K. A Hausdorff chirality measure. *J. Am. Chem. Soc.* **1992**, *114*, 6006−6012.

(19) Buda, A. B.; der Heyde, T. A.; Mislow, K. On Quantifying Chirality. *Angew. Chem., Int. Ed.* **1992**, *31*, 989−1007.

(20) Fernandez-Corbaton, I.; Fruhnert, M.; Rockstuhl, C. Objects of maximum electromagnetic chirality. *Phys. Rev. X* **2016**, *6*, 031013.

(21) Gutsche, P.; Garcia-Santiago, X.; Schneider, P.-I.; McPeak, K. M.; Nieto-Vesperinas, M.; Burger, S. Role of Geometric Shape in Chiral Optics. *Symmetry* **2020**, *12*, 158.

(22) Tung, W.-K. *Group Theory in Physics: an Introduction to Symmetry Principles, Group Representations, and Special Functions in Classical and Quantum Physics*; World Scientific Publishing Company, 1985.

(23) Wheeler, H. A. A helical antenna for circular polarization. *Proc. IRE* **1947**, *35*, 1484−1488.

(24) Gansel, J. K.; Wegener, M.; Burger, S.; Linden, S. Gold helix photonic metamaterials: a numerical parameter study. *Opt. Express* **2010**, *18*, 1059−1069.

(25) Chadha, A. S.; Zhao, D.; Zhou, W. Comparative study of metallic and dielectric helix photonic metamaterial. *Opt. Mater. Express* **2014**, *4*, 2460−2467.

(26) Gutsche, P.; Mäusle, R.; Burger, S. Locally enhanced and tunable optical chirality in helical metamaterials. *Photonics* **2016**, *3*, 60.

(27) Martens, K.; Funck, T.; Santiago, E. Y.; Govorov, A. O.; Burger, S.; Liedl, T. On the origin of chirality in plasmonic meta-molecules. *arXiv preprint arXiv:2110.06689* **2021**, na.

(28) Kuzyk, A.; Schreiber, R.; Fan, Z.; Pardatscher, G.; Roller, E.-M.; Hogele, A.; Simmel, F. C.; Govorov, A. O.; Liedl, T. DNA-based self-assembly of chiral plasmonic nanostructures with tailored optical response. *Nature* **2012**, *483*, 311−314.

(29) Ishikawa, A.; Tanaka, T.; Kawata, S. Negative magnetic permeability in the visible light region. *Phys. Rev. Lett.* **2005**, *95*, 237401.

(30) Mishchenko, M. I.; Travis, L. D.; Lacis, A. A. *Scattering, Absorption, and Emission of Light by Small Particles*; Cambridge University Press, 2002.

(31) Pomplun, J.; Burger, S.; Zschiedrich, L.; Schmidt, F. Adaptive finite element method for simulation of optical nano structures. *Phys. Status Solidi B* **2007**, *244*, 3419−3434.

(32) Burger, S.; Zschiedrich, L.; Pomplun, J.; Schmidt, F. JCMsuite: An Adaptive FEM Solver for Precise Simulations in Nano-Optics. In *Integrated Photonics and Nanophotonics Research and Applications*, Proceedings, Boston, MA, Jul 13−16, 2008, Optica Publishing Group, Boston, MA, 2008; p ITuE4.

(33) Burger, S.; Zschiedrich, L.; Pomplun, J.; Schmidt, F.; Bodermann, B. Fast simulation method for parameter reconstruction in optical metrology. *Proc. SPIE* **2013**, *8681*, 868119.

(34) Lalau-Keraly, C. M.; Bhargava, S.; Miller, O. D.; Yablonovitch, E. Adjoint shape optimization applied to electromagnetic design. *Opt. Express* **2013**, *21*, 21693−21701.

(35) Miller, O. D. Photonic design: From fundamental solar cell physics to computational inverse design. *Ph.D. Thesis*, University of California, Berkeley, 2012.

(36) Hughes, T. W.; Williamson, I. A.; Minkov, M.; Fan, S. Forward-Mode Differentiation of Maxwell's Equations. *ACS Photonics* **2019**, *6*, 3010−3016.

(37) Kollmann, M. Sensitivity Analysis: The Direct and Adjoint Method. *M.Sc. Thesis*, Universitat Linz, 2010.

(38) Dezert, R.; Richetti, P.; Baron, A. Isotropic Huygens dipoles and multipoles with colloidal particles. *Phys. Rev. B* **2017**, *96*, 180201.

(39) Dezert, R.; Richetti, P.; Baron, A. Complete multipolar description of reflection and transmission across a metasurface for perfect absorption of light. *Opt. Express* **2019**, *27*, 26317−26330.

(40) Zambrana-Puyalto, X.; Fernandez-Corbaton, I.; Juan, M.; Vidal, X.; Molina-Terriza, G. Duality symmetry and Kerker conditions. *Opt. Lett.* **2013**, *38*, 1857−1859.

(41) Slivina, E.; Abass, A.; Bätzner, D.; Strahm, B.; Rockstuhl, C.; Fernandez-Corbaton, I. Insights into Backscattering Suppression in Solar Cells from the Helicity-Preservation Point of View. *Phys. Rev. Appl.* **2019**, *12*, 054003.

(42) Mun, J.; Moon, S.-W.; Rho, J. Multipole decomposition for interactions between structured optical fields and meta-atoms. *Opt. Express* **2020**, *28*, 36756−36770.

(43) Waterman, P. Matrix formulation of electromagnetic scattering. *Proc. IEEE* **1965**, *53*, 805−812.

(44) Waterman, P.; McCarthy, C. *Numerical solution of electromagnetic scattering problems*; IEEE, 1968.

(45) Hagemann, F.; Arens, T.; Betcke, T.; Hettlich, F. Solving inverse electromagnetic scattering problems via domain derivatives. *Inv. Prob.* **2019**, *35*, 084005.

(46) Zhan, A.; Fryett, T. K.; Colburn, S.; Majumdar, A. Inverse design of optical elements based on arrays of dielectric spheres. *Appl. Opt.* **2018**, *57*, 1437−1446.

(47) Pelikan, M.; Goldberg, D. E.; Cantú-Paz, E.; et al. BOA: The Bayesian optimization algorithm. In *GECCO'99: Proceedings of the 1st Annual Conference on Genetic and Evolutionary Computation*, Orlando, FLA, Jul 13−17, 1999, Morgan Kaufmann Publishers Inc., San Francisco, CA, 1999; pp 525−532.

(48) Snoek, J.; Larochelle, H.; Adams, R. P. Practical Bayesian optimization of machine learning algorithms. In *Advances in Neural Information Processing Systems 25*, Proceedings of the 26th Annual Conference on Neural Information Processing Systems, Lake Tahoe, NV, Dec 3−6, 2012, Curran Associates, Inc., United States, 2012; pp 2951−2959.

(49) Schneider, P.-I.; Garcia Santiago, X.; Soltwisch, V.; Hammerschmidt, M.; Burger, S.; Rockstuhl, C. Benchmarking five global optimization approaches for nano-optical shape optimization and parameter reconstruction. *ACS Photonics* **2019**, *6*, 2726−2733.

(50) Williams, C.; Rasmussen, C. E. *Gaussian Processes for Machine Learning*; MIT Press: Cambridge, MA, 2006; Vol. 2.

(51) Solak, E.; Murray-smith, R.; Leithead, W.; Leith, D.; Rasmussen, C. Derivative Observations in Gaussian Process Models of Dynamic Systems. In *Advances in Neural Information Processing Systems 15*, Proceedings of the 15th International Conference on Neural Information Processing Systems (NIPS 02), British Columbia, Canada, Dec 9−14, 2002, MIT Press, Cambridge, MA, 2003.

(52) Wu, J.; Poloczek, M.; Wilson, A. G.; Frazier, P. Bayesian Optimization with Gradients. In *Advances in Neural Information Processing Systems 30*, Proceedings of the 31st Annual Conference on Neural Information Processing Systems (NIPS 2017), Long Beach, CA, Dec 4−9, 2017, Curran Associates, Inc., United States, 2017.

(53) McPeak, K. M.; Jayanti, S. V.; Kress, S. J.; Meyer, S.; Iotti, S.; Rossinelli, A.; Norris, D. J. Plasmonic films can easily be better: rules and recipes. *ACS Photonics* **2015**, *2*, 326−333.

(54) Hagemann, H.-J.; Gudat, W.; Kunz, C. Optical constants from the far infrared to the x-ray region: Mg, Al, Cu, Ag, Au, Bi, C, and $Al_2O_3$. *J. Opt. Soc. Am.* **1975**, *65*, 742−744.

(55) Novotny, L. Effective wavelength scaling for optical antennas. *Phys. Rev. Lett.* **2007**, *98*, 266802.

(56) Jones, D. S. A thin wire approximation. *SIAM J. Appl. Math* **1990**, *50*, 547−558.

(57) Fernandez-Corbaton, I.; Zambrana-Puyalto, X.; Tischler, N.; Vidal, X.; Juan, M. L.; Molina-Terriza, G. Electromagnetic duality symmetry and helicity conservation for the macroscopic Maxwell's equations. *Phys. Rev. Lett.* **2013**, *111*, 060401.

(58) Fernandez-Corbaton, I.; Beutel, D.; Rockstuhl, C.; Pausch, A.; Klopper, W. Computation of electromagnetic properties of molecular ensembles. *ChemPhysChem* **2020**, *21*, 878−887.

(59) Höflich, K.; Feichtner, T.; Hansjürgen, E.; Haverkamp, C.; Kollmann, H.; Lienau, C.; Silies, M. Resonant behavior of a single plasmonic helix. *Optica* **2019**, *6*, 1098−1105.

(60) Klein, M. W.; Enkrich, C.; Wegener, M.; Soukoulis, C. M.; Linden, S. Single-slit split-ring resonators at optical frequencies: limits of size scaling. *Opt. Lett.* **2006**, *31*, 1259−1261.

(61) Zhou, J.; Koschny, T.; Kafesaki, M.; Economou, E. N.; Pendry, J. B.; Soukoulis, C. M. Saturation of the magnetic response of split-ring resonators at optical frequencies. *Phys. Rev. Lett.* **2005**, *95*, 223902.

(62) Qiu, J.-H.; Zhou, P.; Gao, X.-Y.; Yu, J.-N.; Wang, S.-Y.; Li, J.; Zheng, Y.-X.; Yang, Y.-M.; Song, Q.-H.; Chen, L.-Y. Ellipsometric study of the optical properties of silver oxide prepared by reactive magnetron sputtering. *J. Korean Phys. Soc.* **2005**, *46*, 269.

(63) Höflich, K.; Yang, R. B.; Berger, A.; Leuchs, G.; Christiansen, S. The Direct Writing of Plasmonic Gold Nanostructures by Electron-Beam-Induced Deposition. *Adv. Mater.* **2011**, *23*, 2657−2661.

(64) Wozniak, P.ł; De Leon, I.; Hoflich, K.; Haverkamp, C.; Christiansen, S.; Leuchs, G.; Banzer, P. Chiroptical response of a single plasmonic nanohelix. *Opt. Express* **2018**, *26*, 19275−19293.

(65) Fazel-Najafabadi, A.; Auguié, B. Orientation dependence of optical activity in light scattering by nanoparticle clusters. *arXiv preprint arXiv:2111.00997* **2021**, na.

(66) Mallet, P.; Guérin, C. A.; Sentenac, A. Maxwell-Garnett mixing rule in the presence of multiple scattering: Derivation and accuracy. *Phys. Rev. B* **2005**, *72*, 014205.

(67) Werdehausen, D.; Santiago, X. G.; Burger, S.; Staude, I.; Pertsch, T.; Rockstuhl, C.; Decker, M. Modeling Optical Materials at the Single Scatterer Level: The Transition from Homogeneous to Heterogeneous Materials. *Advanced Theory and Simulations* **2020**, 3, 2000192.

(68) Sihvola, A.; Lindell, I. Analysis on Chiral Mixtures. *Journal of Electromagnetic Waves and Applications* **1992**, *6*, 553−572.

(69) Chern, R.-L. Wave propagation in chiral media: composite Fresnel equations. *Journal of Optics* **2013**, *15*, 075702.

(70) Arens, T.; Hagemann, F.; Hettlich, F.; Kirsch, A. The definition and measurement of electromagnetic chirality. *Math. Meth. Appl. Sci.* **2018**, *41*, 559−572.

(71) Capdeboscq, Y.; Griesmaier, R.; Knöller, M. An Asymptotic Representation Formula for Scattering by Thin Tubular Structures and an Application in Inverse Scattering. *Multiscale Model. Simul.* **2021**, *19*, 846−885.

(72) Arens, T.; Griesmaier, R.; Knöller, M. Maximizing the Electromagnetic Chirality of Thin Dielectric Tubes. *SIAM J. Appl. Math* **2021**, *81*, 1979−2006.

(73) Fernandez Corbaton, I. Helicity and duality symmetry in light matter interactions: Theory and applications. *Ph.D. thesis*, Macquarie University, Faculty of Science and Engineering, Department of Physics and Astronomy, 2014.

(74) Demésy, G.; Auger, J.-C.; Stout, B. Scattering matrix of arbitrarily shaped objects: combining finite elements and vector partial waves. *J. Opt. Soc. Am. A* **2018**, *35*, 1401−1409.

(75) Garcia-Santiago, X.; Hammerschmidt, M.; Burger, S.; Rockstuhl, C.; Fernandez-Corbaton, I.; Zschiedrich, L. Decomposition of scattered electromagnetic fields into vector spherical wave functions on surfaces with general shapes. *Phys. Rev. B* **2019**, *99*, 045406.

(76) Nogueira, F. Bayesian Optimization: Open source constrained global optimization tool for Python, 2014; https://github.com/fmfn/BayesianOptimization.

(77) Bergstra, J.; Yamins, D.; Cox, D. D. Making a Science of Model Search: Hyperparameter Optimization in Hundreds of Dimensions for Vision Architectures. In *Proceedings of the 30th International Conference on Machine Learning*, Atlanta, GA, Jun 16−21, 2013, JMLR: W&CP, 2013; pp 115−123.

(78) Pedregosa, F.; et al. Scikit-learn: Machine Learning in Python. *Journal of Machine Learning Research* **2011**, *12*, 2825−2830.

(79) Danka, T.; Horvath, P. modAL: A modular active learning framework for Python. *arXiv 1805.00979* **2018**, na.

(80) Jackson, J. D. *Classical Electrodynamics*; Wiley, 1999.

(81) Jones, D. R. A taxonomy of global optimization methods based on response surfaces. *J. Glob. Optim.* **2001**, *21*, 345−383.

(82) Hennig, P.; Schuler, C. J. Entropy search for information-efficient global optimization. *Journal of Machine Learning Research* **2012**, *13*, 1809−1837.

(83) Mark, A. G.; Gibbs, J. G.; Lee, T.-C.; Fischer, P. Hybrid nanocolloids with programmed three-dimensional shape and material composition. *Nat. Mater.* **2013**, *12*, 802−807.

(84) Glass, R.; Möller, M.; Spatz, J. P. Block copolymer micelle nanolithography. *Nanotechnology* **2003**, *14*, 1153.